Title

Understanding and Controlling Anionic Electrochemical Activity in High-Capacity Oxides for Next Generation Li-Ion Batteries

Journal

Chemistry of Materials, 29(3)

ISSN

0897-4756

Authors

Qiu, Bao
Zhang, Minghao
Xia, Yonggao
et al.

Publication Date

2017-02-14

DOI

10.1021/acs.chemmater.6b04815

Peer reviewed

CHEMISTRY OF MATERIALS
Cite This: Chem. Mater. XXXX, XXX, XXX−XXX
Article
pubs.acs.org/cm

Understanding the Electrochemical Mechanisms Induced by Gradient Mg^{2+} Distribution of Na-Rich $Na_{3+x}V_{2-x}Mg_x(PO_4)_3$/C for Sodium Ion Batteries

Hui Li,[†,‡,§] Hanmei Tang,[‡] Chuze Ma,[‡] Ying Bai,[*,†] Judith Alvarado,[‡,#] Balachandran Radhakrishnan,[‡] Shyue Ping Ong,[*,‡] Feng Wua,[∥] Ying Shirley Meng,[*,‡] and Chuan Wu[*,†,∥]

[†]Beijing Key Laboratory of Environmental Science and Engineering, School of Materials Science and Engineering, Beijing Institute of Technology, Beijing 100081, China

[‡]Department of NanoEngineering, University of California San Diego, La Jolla, California 92093, United States

[§]State Key Laboratory of Advanced Transmission Technology, Global Energy Interconnection Research Institute Co. Ltd., Beijing 102211, China

[∥]Collaborative Innovation Center of Electric Vehicles in Beijing, Beijing 100081, China

Supporting Information

ABSTRACT: Metal-ion doping can improve the electrochemical performance of $Na_3V_2(PO_4)_3$. However, the reason for the enhanced electrochemical performance and the effects of cation doping on the structure of $Na_3V_2(PO_4)_3$ have yet been probed. Herein, Mg^{2+} is doped into $Na_3V_2(PO_4)_3$/C according to the first-principles calculation. The results indicate that Mg^{2+} prefers to reside in the V site and an extra electrochemical active Na^+ is introduced to the $Na_3V_2(PO_4)_3$/C crystal to maintain the charge balance. The distribution of Mg^{2+} in the particle of $Na_3V_2(PO_4)_3$/C is further studied by electrochemical impedance spectroscopy. We find that the highest distribution of Mg^{2+} on the surface of the particles leads to facile surface electrochemical reactions for Mg^{2+}-doped samples, especially at high rates.

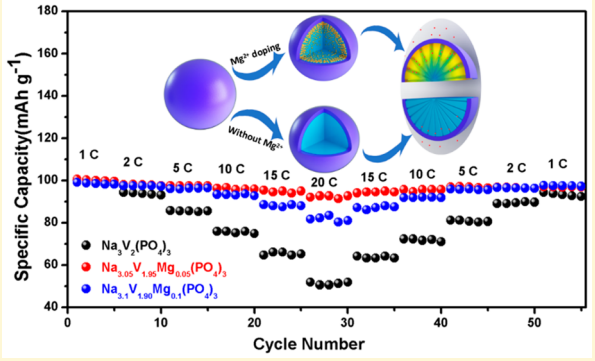

1. INTRODUCTION

Because of the low cost and abundance of sodium element in the Earth's crust, sodium ion batteries (SIBs) are now attracting more attention for grid-scale energy storage applications.[1−4] In addition, because of the lower half-reaction potential of SIBs than that of lithium ion batteries (LIBs),[5] SIBs can be used in electrolyte systems with lower decomposition potential such as water-based electrolytes, which makes it inexpensive compared to LIBs. Recently, SIBs have been investigated extensively including cathodes, anodes, and electrolytes. However, practical applications of SIBs are limited because of the larger ionic radius of the sodium ion compared to that of the lithium ion (1.02 Å for Na^+ vs 0.76 Å for Li^+) and higher equivalent weight of Na than that of Li.[6,7] Thus, it is necessary to find more suitable electrode materials with good structural stability and electrochemical performance to enable more SIB applications.

Because of the highly covalent three-dimensional framework that generates large interstitial space where sodium ions may easily diffuse during the charging/discharging process,[8−12] NASICON-structured compounds are considered as prospective cathode material for sodium ion batteries[13−15] and hybrid ion batteries.[16] Among various sodium super ion conductor (NASICON)-structured compounds, $Na_3V_2(PO_4)_3$ shows superior performances. It is worth mentioning that $Na_3V_2(PO_4)_3$ possesses a rhombohedral $R\bar{3}C$ symmetry which benefits sodium ion diffusion. Moreover, $Na_3V_2(PO_4)_3$ displays a high voltage plateau (3.4 V) that is relatively higher than that of most other Na ion battery (NIB) cathode materials.[17] The high specific energy density (~400 W·h/kg) and high thermal stability of $Na_3V_2(PO_4)_3$ are suitable for large-scale energy storage.[18,19]

Although $Na_3V_2(PO_4)_3$ has many advantages, low electrical conductivity (similar to $Li_3V_2(PO_4)_3$ and $LiFePO_4$) significantly limits its electrochemical performance.[20−22] Until now, coating various carbon materials, reducing the particle size, and doping metal ions have been adopted to improve the electrochemical performance and cation doping is an effective and simple way to modify $Na_3V_2(PO_4)_3$. Mg^{2+},[23] Fe^{3+},[24] Cr^{3+},[25] Al^{3+},[26] Mn^{2+},[27,28] K^+,[29] and Ni^{2+}[30] have been doped into $Na_3V_2(PO_4)_3$. The results show that all doped samples display enhanced electrochemical performance. However, most of the papers were committed to improving the electrochemical

Received: October 17, 2017
Revised: April 3, 2018
Published: April 3, 2018

DOI: 10.1021/acs.chemmater.7b03903
Chem. Mater. XXXX, XXX, XXX−XXX

performance, while the mechanistic understanding on the effects of cation doping of $Na_3V_2(PO_4)_3$ is still ambiguous and not comprehensive.

In this work, we first use density functional theory (DFT) method to determine the most preferred doping mechanism for Mg. Then we implemented a screening process to identify all possible divalent dopants under this mechanism. We find the following: (1) Mg^{2+} tends to substitute on the V site and extra sodium ions are introduced to keep the charge neutral; (2) Ni^{2+}- and Mg^{2+}-doped structures are of the highest chemical stability, which corresponds with our initial guess; and (3) the cost-effective Mg ion was chosen to be doped into $Na_3V_2(PO_4)_3$. To further determine the optimal doping concentration of Mg^{2+}, where computational screening is hindered by the max atom number of the unit cell, a series of Mg^{2+}-doped Na-rich $Na_{3+x}V_{2-x}Mg_x(PO_4)_3/C$ (x = 0, 0.05, and 0.1) were synthesized by the sol−gel method. The effects of Mg^{2+} doped on the crystal structure, Mg^{2+} doping site, and the distribution of Mg^{2+} within the particles for the electrochemical performance will be discussed further in detail.

2. METHODS

2.1. Sample Preparation. All $Na_{3+x}V_{2-x}Mg_x(PO_4)_3/C$ (x = 0, 0.05, and 0.1) samples were synthesized by the sol−gel method. Stoichiometric amounts of NaOH, NH_4VO_3, $NH_4H_2PO_4$, $Mg(CH_3COO)_2$, and citric acid were used as raw materials. First, NH_4VO_3 was dissolved in deionized water and stirred at 80 °C. Citric acid solution, NaOH solution, $Mg(CH_3COO)_2$ solution, and $NH_4H_2PO_4$ solution were added into the above NH_4VO_3 solution while stirring everything at 80 °C. After several hours, all the water evaporated and the solution subsequently turned into a gel. The gel was calcinated at 800 °C in the flowing argon atmosphere for 8 h to obtain $Na_{3+x}V_{2-x}Mg_x(PO_4)_3/C$ with the respected composition (x = 0, 0.05, and 0.1). All chemicals were used directly without any further purification.

2.2. Characterization. X-ray diffraction (XRD) measurements on all the materials were performed using Cu Kα radiation to identify the crystalline phase. Rietveld refinement was performed using FullProf software. Na-ion conductivity was measured with electrochemical impedance spectroscopy using an impedance analyzer Solartron 1255B) in the frequency range of 100 kHz to 10 mHz at 25, 50, and 60 °C. Inductively coupled plasma (ICP) analysis was performed using a PerkinElmer 3700 optical emission plasma spectrometer.

The structure of the Na-rich $Na_{3.05}V_{1.95}Mg_{0.05}(PO_4)_3/C$ sample was investigated by using a FEI Tecnai G2 F20 transmission electron microscope equipped with selected area electrode diffraction patterns and the scanning transmission electron microscope (STEM) operated at 200 kV.

2.3. Computational Methods. *2.3.1. Density Functional Theory Calculations.* All density functional theory (DFT) calculations were performed using Vienna Ab initio Simulation Package[31] within the projector augmented wave method.[32] The Perdew−Burke−Ernzerhof generalized gradient approximation[33] with Hubbards correction (GGA +U) was used for the exchange-correlation functional. For all DFT energy calculations, a plane-wave cutoff of 520 eV and a k-point density of at least 1000/(number of atoms in unit cell) and spin-polarized condition were used for all cases. All structure manipulations and postanalysis were carried out using Python Materials Genomics (Pymatgen)[34] package.

2.3.2. Structure Generation. The initial disordered structure was obtained from Inorganic Crystal Structure Database (ICSD)[35] ($Na_{3.803}V_{2.5}(PO_4)_3$: ICSD no. 248140). The lowest energy structure was identified by computing the ground-state energy of all symmetrically distinct atomic configurations[36] enumerated using the algorithm of Hart and Forcade.[37]

For doped chemistries, all symmetrically distinct ordering of $Na_{3+x}V_{2-x}M_x(PO_4)_3$ and $Na_3V_{2-x}M_x(PO_4)_3$ were enumerated using the aforementioned algorithm for x = 0.0625, 0.125, 0.25, and 0.5.

2.3.3. Divalent Dopants Selections. Some divalent ions are not suitable for dopants; thus, they are excluded: (1) Radioactive elements: Tc and Pm and from Bi to the end of the periodic table. (2) Nobel metals: Rh, Ir, Pt, and Au. (3) Elements with toxicity: Cd and Hg. (4) Elements where the divalent state is not available: alkali metals, noble gases, etc. As a result, Ni, Mg, Cu, Cr, Zn, Pd, Ag, Ca, Sr, and Ba are selected as potential dopants.

2.3.4. Phase Stability and Dopant Formation Energy. The phase stability of a given compound $Na_xV_yP_zO_uM_v$ (M is the dopant species) was estimated using the energy above the convex hull (E_{hull})[38] in the corresponding Na−V−P−O−M phase diagram. Precomputed data used in phase diagram construction were all obtained from the Materials Project (MP)[39] database using the Materials Project API.[40] The E_{hull} value of stable phases is 0 meV/atom. The higher the E_{hull} is, the less stable the compound is predicted to be. In this work, an E_{hull} value of 20 meV/atom is chosen as the cutoff value beyond which the chemistry is considered to be unstable to be synthesized.

The neutral dopant formation energy was calculated using the formalism reported by Wei et al.,[41] which indicates the dopability of divalent dopant M^{2+} into the host NASICON material. The computational details are similar to the previous report.[42] Specifically, the dopant formation energy is calculated using the formalism:

$$E_f[M] = E_{tot}[M] - E_{tot}[bulk] - \sum_i n_i\mu_i$$

where $E_{tot}[M]$ and $E_{tot}[bulk]$ are the total energies of the structure with and without the neutral dopant M, respectively. n_i is the number of species i that is being added ($n_i > 0$) or removed ($n_i < 0$). μ_i is the atomic chemical potential of species i that varies based on different experimental conditions. In this work, the lower bound of the dopant formation energy was calculated, which is equal to the difference of decomposition energies between the doped and host materials.

2.4. Electrochemical Tests. Electrochemical measurements of $Na_{3+x}V_{2-x}Mg_x(PO_4)_3/C$ (x = 0, 0.05, and 0.1) samples were carried out using CR2016 coin cells. Na metal was used as the counter electrode. The electrodes were made by mixing the active material, carbon black, and poly(vinylidene fluoride) in an 8:1:1 ratio. Then the electrodes were dried at 100 °C for 10 h. Afterward, 10 mm diameter circular disk electrodes were cut to form the electrode. The mass loading of the active material on the electrode was about 4.0 mg cm^{-2}. The cells were cycled in 1 M $NaPF_6$ in PC while using glass fiber (Whatman GF/F) as the separator. Galvanostatic experiments were carried out using an Arbin BT2000 battery testing system. The voltage range was maintained between 2.5 and 4.0 V. Before the galvanostatic charging/discharging tests, the batteries underwent an aging process for over 2 h to make sure $Na_{3+x}V_{2-x}Mg_x(PO_4)_3/C$ (x = 0, 0.05, and 0.1) was fully soaked by the electrolyte.

3. RESULTS AND DISCUSSION

All synthesized samples $Na_{3+x}V_{2-x}Mg_x(PO_4)_3/C$ (x = 0, 0.05, and 0.1) were found to crystallize in the NASICON structure ($R\bar{3}C$ space group, rhombohedral unit with 2 Na in 18e position and 1 Na in 6b position). The XRD patterns are shown in Figure 1 and the Rietveld analysis of the sample with x = 0 and 0.05 are reproduced in Figure 2. The refinement was done by the FullProf program.[23,30] Figure 2 shows that the calculated pattern matches well with the observed pattern. The structural parameters of $Na_3V_2(PO_4)_3/C$ and $Na_{3.05}V_{1.95}Mg_{0.05}(PO_4)_3/C$ phases as determined from the Rietveld refinement are illustrated in Table 1. The reasonably small R factors show that a single phase was obtained and no impurity phases were detected at the resolution of our X-ray diffractometer.

DOI: 10.1021/acs.chemmater.7b03903
Chem. Mater. XXXX, XXX, XXX−XXX

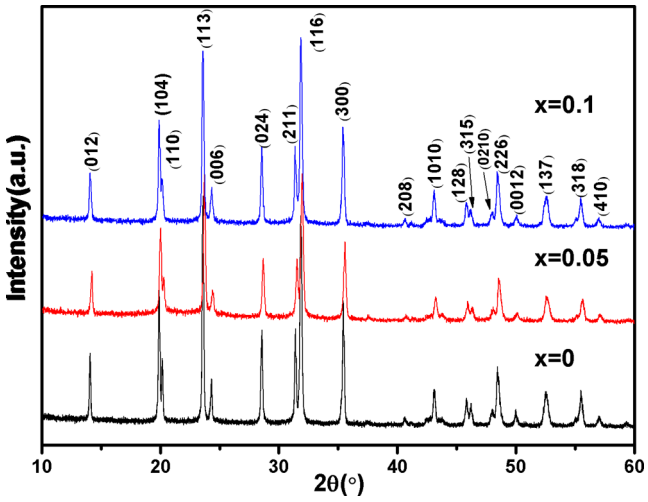

Figure 1. XRD patterns of $Na_{3+x}V_{2-x}Mg_x(PO_4)_3/C$ (x = 0, 0.05, and 0.1).

To confirm that Mg^{2+} doping can improve the $Na_3V_2(PO_4)_3$ performance, electrochemical measurements of $Na_{3+x}V_{2-x}Mg_x(PO_4)_3/C$ (x = 0, 0.05, and 0.1) samples were carried out, as shown in Figure 3. The cycle performance at 1 and 10 C are displayed in parts (a) and (b), respectively, of Figure 3. It is clear that Mg^{2+}-doped samples present superior cycle performance at both 1 and 10 C. When cycled at 1 C, all the samples deliver similar initial specific capacity; however, after 180 cycles the capacity of $Na_{3.05}V_{1.95}Mg_{0.05}(PO_4)_3/C$ is almost 10 mA h g^{-1} higher than that of $Na_3V_2(PO_4)_3/C$. When cycled at 10 C, the difference in electrochemical performance between undoped sample and Mg^{2+}-doped sample are more evident. For $Na_{3.05}V_{1.95}Mg_{0.05}(PO_4)_3/C$, the initial capacity is 96.7 mA h g^{-1}, and it has a capacity retention of 88.9% after 180 cycles. However, the undoped $Na_3V_2(PO_4)_3/C$ can deliver only 88.8 and 63 mA h g^{-1} at the first cycle and after 180 cycles, respectively.

The rate performance is shown in Figure 3c. It is obvious that the rate ability of Mg^{2+}-doped $Na_3V_2(PO_4)_3/C$ is better than that of the undoped sample. $Na_{3.05}V_{1.95}Mg_{0.05}(PO_4)_3/C$ delivers 95.5 and 92.1 mA h g^{-1} at 15 and 20 C, respectively, whereas $Na_3V_2(PO_4)_3/C$ delivers only 64.7 and 50.6 mA h g^{-1} at the same rates. The above results demonstrate that doping can improve the electrochemical performance. In addition, it is found that the higher the rate, the greater the difference in the electrochemical performance between the Mg^{2+}-doped sample and the undoped sample.

The reason for the enhanced electrochemical performance of the doped samples is explored. According to previous reports,[43,44] there are Na site and V site for $Na_3V_2(PO_4)_3$ to substitute. There are also two Na sites for $Na_3V_2(PO_4)_3$ and the crystal structure is displayed in Figure S1 of the Supporting Information. Na(1) site has sixfold coordination situated between two adjacent $V_2(PO_4)_3$ units along the z axis. Na(2) site has eightfold coordination located at the same z value as the phosphorus atoms between two PO_4 tetrahedra. For each formula, there are three positions for Na(2) and one position for Na(1). The sodium ions at the Na(2) site are electrochemically active when $Na_3V_2(PO_4)_3$ is used as cathode of SIBs. For $Na_3V_2(PO_4)_3$, two of the three sodium ions are in the Na(2) site and the remaining sodium ions are located in the Na(1) site. Because of the different valences among Mg^{2+}, V^{3+}, and Na^+, the molar ratio of V^{3+} and Na^+ is changed to keep the charge balance when Mg^{2+} migrates to a different site. Because of the complexity of the crystal structure and the valence of the elements, identifying the doping site is vital to understand how the dopant influences the electrochemical properties. Three mechanisms of Mg^{2+}-doped $Na_3V_2(PO_4)_3$ are studied and illustrated in Table 2. The detailed crystal structure corresponding to the different mechanisms is shown in Figure 4. In Figure 4a, one Na^+ in the Na(2) site disappears when a Mg^{2+} replaces one Na^+ because of the lower valence of Na^+ compared to that of Mg^{2+}. As a result, the electrochemically active Na decreases as Mg^{2+} increases and moves to the Na site. In mechanism 2, charge compensation is achieved by a V^{3+} becoming V^{4+}, which reduces the available redox couples for storage. Finally, in mechanism 3, an additional Na^+ is introduced to the Na(2) site (Figure 4c) when Mg^{2+} is doped into the V site and V^{3+} does not change the valence; hence, more electrochemical Na^+ is inserted into the crystal. To determine which mechanism happens in this work, several methods are used and discussed below.

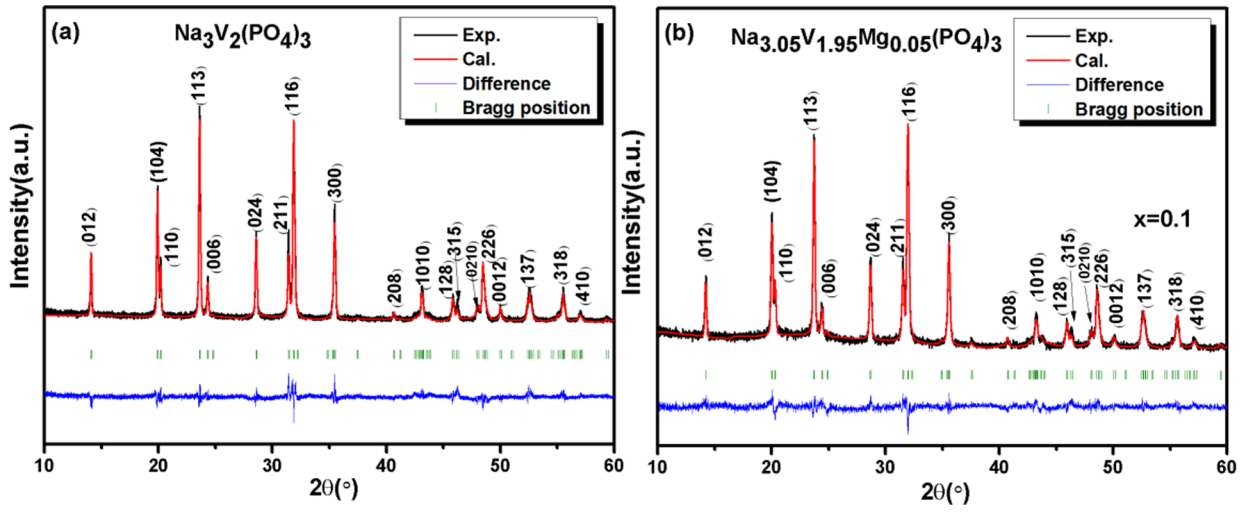

Figure 2. XRD Rietveld refinement results of (a) $Na_3V_2(PO_4)_3/C$ and (b) $Na_{3.05}V_{1.95}Mg_{0.05}(PO_4)_3/C$.

DOI: 10.1021/acs.chemmater.7b03903
Chem. Mater. XXXX, XXX, XXX−XXX

Table 1. Structural Parameters of $Na_3V_2(PO_4)_3$/C and $Na_{3.05}V_{1.95}Mg_{0.05}(PO_4)_3$/C Determined from XRD Rietveld Refinement

							occupancy			
	$a(=b)$	c	V	R_p (%)	R_{wp} (%)	R_b (%)	Na1	Na2	V	Mg
$Na_3V_2(PO_4)_3$	8.72204	21.802	1436.374	5.34	6.91	6.47	1.00000	2.00000	2.08000	0
$Na_{3.05}V_{1.95}Mg_{0.05}(PO_4)_3$	8.72277	21.833	1438.004	4.69	===6.26	9.29	0.98156	2.05971	1.95005	0.04995

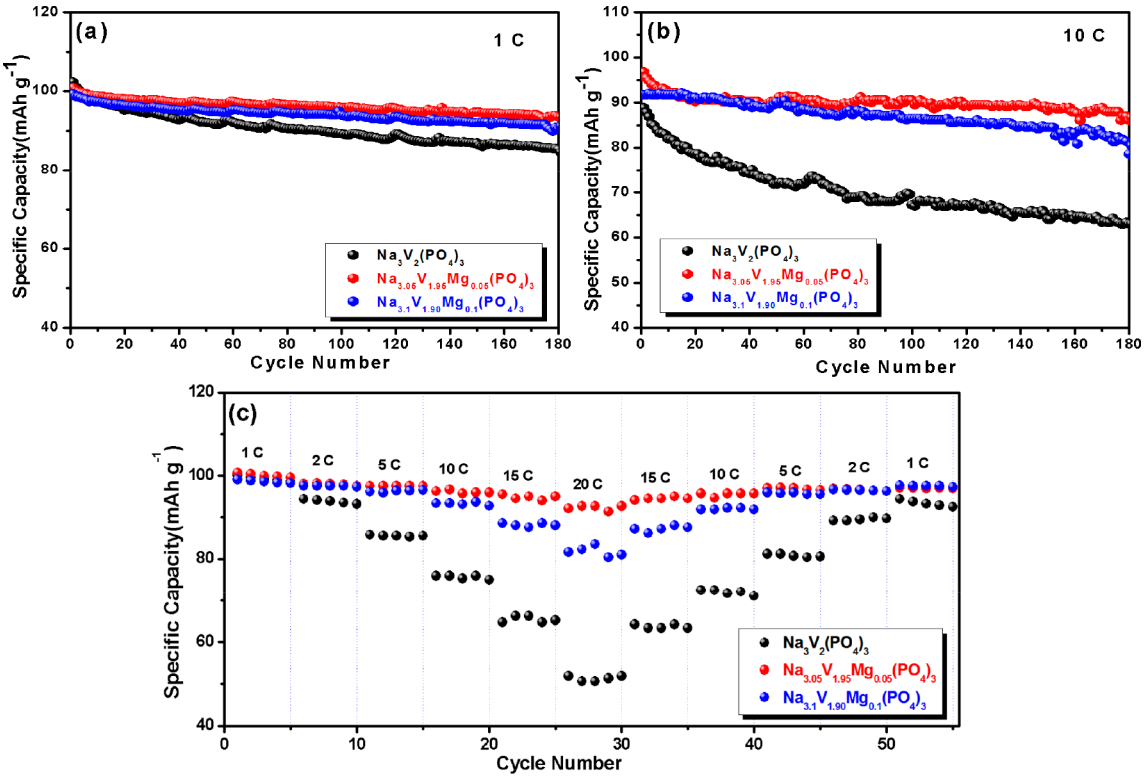

Figure 3. Electrochemical performance of $Na_{3+x}V_{2-x}Mg_x(PO_4)_3$/C ($x$ = 0, 0.05, and 0.1): (a) cycle performance at 1 C, (b) cycle performance at 10 C, and (c) rate performance.

Table 2. Mechanisms of Mg^{2+}-Doped $Na_3V_2(PO_4)_3$

	mechanism 1	mechanism 2	mechanism 3
doping site	Na site	V site (V valence changes)	V site (Na is introduced)
compd	$Na_{3-2x}V_2Mg_x(PO_4)_3$	$Na_3V_{2-x}Mg_x(PO_4)_3$	$Na_{3+x}V_{2-x}Mg_x(PO_4)_3$

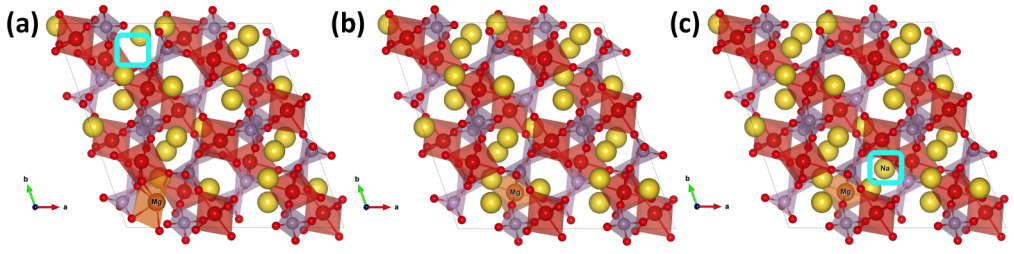

Figure 4. Crystal structure of $Na_3V_2(PO_4)_3$ by first-principles calculation: (a) when Mg^{2+} goes to the Na site, (b) when Mg^{2+} goes to the V site and V^{3+} changes the valence to keep charge balance, and (c) when Mg^{2+} goes to the V site and more Na^+ are introduced to keep the charge balance.

Li et al.[45] proposed an effective way to explore the preferred doping site in polyanion materials. Their formula is shown as follow:

$$D_{M1(2)} = |(X_M - X_{M1(2)})/X_{M1(2)}| + |(r_M - r_{M1(2)})/r_{M1(2)}|$$

where X_M and $X_{M1(2)}$ are electronegativity values of the dopant and the substituted ion and r_M and $r_{M1(2)}$ are the ionic radius of the dopant and the substituted ion. If $D_{M1} < D_{M2}$, the dopant tends to go to the M1 site, while if $D_{M1} > D_{M2}$, the dopant prefers to occupy the M2 site. According to the above formula, the values for Mg^{2+}-doped $Na_3V_2(PO_4)_3$/C are D_V = 0.3228 and D_{Na} = 0.521. Mg^{2+} goes to the V site for Mg^{2+}-doped $Na_3V_2(PO_4)_3$/C since D_{Na} is greater than D_V.

The doping site was studied by first-principles calculations. Table 3 shows the phase stability represented by E_{hull} with respect to the different Mg^{2+} doping mechanism. Mechanism 3

DOI: 10.1021/acs.chemmater.7b03903
Chem. Mater. XXXX, XXX, XXX−XXX

Table 3. E_{hull} (meV/atom) and E_f (meV/f.u.) for Different Doping Sites of Mg^{2+} in $Na_3V_2(PO_4)_3$

	$Na_{3-2x}V_2Mg_x(PO_4)_3$ [a]		$Na_3V_{2-x}Mg_x(PO_4)_3$ [b]		$Na_{3+x}V_{2-x}Mg_x(PO_4)_3$ [c]	
	E_{hull}	E_f	E_{hull}	E_f	E_{hull}	E_f
$x = 0.0625$	0	0	1.92	613.86	0	0
$x = 0.125$	1.51	239.59	3.14	502.36	0.47	75.46
$x = 0.25$	4.63	365.89	4.45	356.17	0.21	16.66
$x = 0.5$	10.74	418.93	4.77	190.61	0	0

[a]Mechanism 1, Na site. [b]Mechanism 2, V site (V valence changes). [c]Mechanism 3, V site (Na is introduced).

is most probable as shown in Table 3. Mg^{2+} is inclined to go to the V site, which is consistent with the above empirical formula. It can be concluded that more Na^+ is introduced to the crystal structure to keep the charge balance.

On the basis of the above results, first-principles calculations were carried out only under mechanism 3 to find potential doping species and the preferred doping concentration among divalent ions [Ni^{2+}, Mg^{2+}, Cu^{2+}, Cr^{2+}, Zn^{2+}, Pd^{2+}, Ag^{2+}, Ca^{2+}, Sr^{2+}, and Ba^{2+}]. The chemical stability and doping concentration (x = 0.0625, 0.125, 0.25, and 0.5) relationship for both mechanisms are shown in Figure 5, which indicates that the

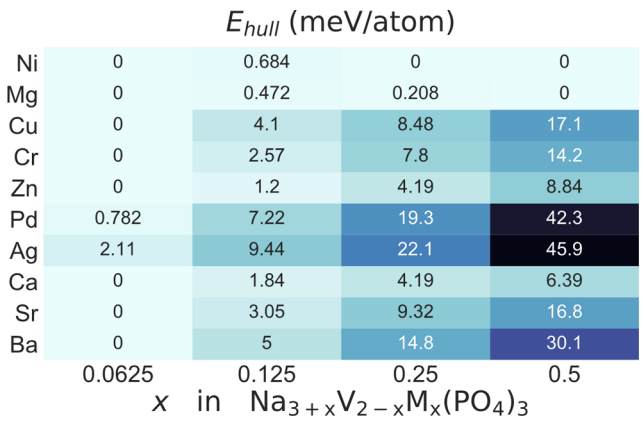

Figure 5. Chemical stability (E_{hull}) of substitutional divalent dopants in $Na_3V_2(PO_4)_3$. To maintain charge balance after substitution on V sites, extra sodium ions are introduced.

phase stability decreases as dopant concentrates. However, Mg^{2+}-doped chemistries remain relatively stable within the tested dopant concentrations. This observed stability may be due to the similar ionic radius of Mg^{2+} (86 pm) and V^{3+} (78 pm), which alleviates the structural distortion from doping.

All the theoretical results above show that Mg^{2+} prefers to go to the V site and the doping site was proved by an experimental method. Because of the different valence numbers between Mg^{2+}, V^{3+}, and Na^+, the molar ratio of V and Na is changed to keep the charge balance when Mg^{2+} goes to the different sites as discussed above. Table S1 and Table S2 illustrate the theoretical ratios of Na, V, Mg, and P for different doping sites. The real compositions of undoped and Mg^{2+}-doped $Na_3V_2(PO_4)_3$/C were explored by ICP and the results are displayed in Table S3. The comparison of the Na/V ratio trend for different doping sites is displayed in Figure 6. It is found that the Na/V trend from ICP is consistent with the Na/V ratio of theoretical value (Mg^{2+} is doped on V site). The experimental results demonstrate that Mg^{2+} goes to the V site

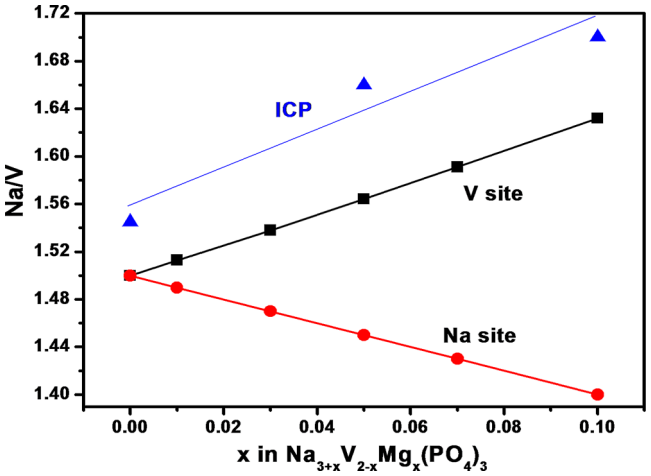

Figure 6. Na/V ratio for Mg^{2+}-doped $Na_3V_2(PO_4)_3$/C when doped at different sites and Na/V ratio for the ICP results.

and more Na^+ is introduced to $Na_3V_2(PO_4)_3$ crystal structure to keep the charge balance. Hence, Mg^{2+}-doped $Na_3V_2(PO_4)_3$/C shows better electrochemical performance because inserting excess Na^+ is electrochemically active during the charging/discharging process.

To explain the reason for the enhanced electrochemical performance at high rates for Mg^{2+}-doped $Na_3V_2(PO_4)_3$/C, the crystal structure and kinetic properties were investigated in detail. The unit cell volumes of $Na_{3+x}V_{2-x}Mg_x(PO_4)_3$ from first-principles calculation are provided in Table 4. When x increases

Table 4. Volume of $Na_{3+x}V_{2-x}Mg_x(PO_4)_3$ from First-Principles Calculations

sample	$x = 0$	$x = 0.0625$	$x = 0.125$	$x = 0.25$
V	1438.74	1499.52	1502.19	1504.62

from 0 to 0.0625, the volume increases from 1438.74 to 1499.52, that is, by 4%. However, the XRD refinement results show a volume increase from 1436.374 to 1438.004 when x increases from 0 to 0.05, which is only about 0.1% of the volume change. It is worth noting that the model from calculation is built based on the uniform distribution of Mg^{2+}. From the noticeable difference of volume changes between first-principles calculation and XRD Rietveld refinement, it can be inferred that Mg^{2+} is not evenly distributed in the bulk.

To verify this assumption, the internal resistance of sodium half cell assembled with $Na_3V_2(PO_4)_3$/C and $Na_{3.05}V_{1.95}Mg_{0.05}(PO_4)_3$/C were evaluated. The Nyquist plots are shown in Figure 7. In the Nyquist plots, each impedance spectrum consists of a depressed semicircle at high frequency and a slope line in the low-frequency range. The high-frequency region of the semicircle is attributed to interfacial resistance between the electrode and the electrolyte (ion migration through the surface layer and the charge-transfer reaction through the electrode−electrolyte interphase), while the slope line is due to Warburg impedance, which originates from the diffusion of sodium ions into the bulk of the electrode material.[46−48] In Figure 7a, the semicircle is hardly changed at different temperatures in $Na_3V_2(PO_4)_3$/C; however, when Mg^{2+} is doped into $Na_3V_2(PO_4)_3$, the interfacial resistance decreases as the temperature increases, shown in Figure 7b. It can be concluded that Mg^{2+} doping has a significant impact on

DOI: 10.1021/acs.chemmater.7b03903
Chem. Mater. XXXX, XXX, XXX−XXX

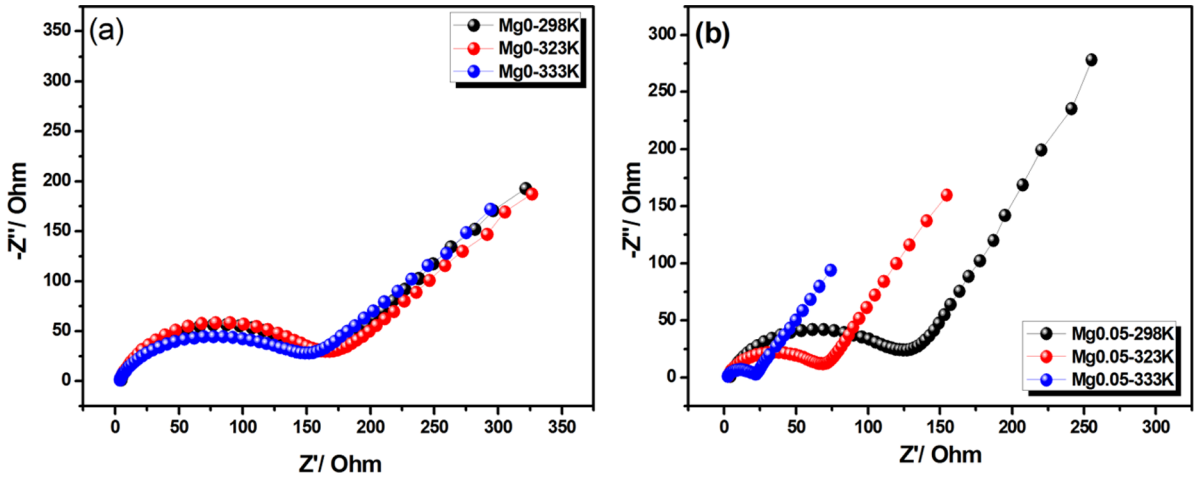

Figure 7. Nyquist plots of (a) $Na_3V_2(PO_4)_3/C$ and (b) $Na_{3.05}V_{1.95}Mg_{0.05}(PO_4)_3/C$ at 298 K (black), 323 K (red), and 333 K (blue).

the interface of $Na_3V_2(PO_4)_3/C$. Furthermore, the sodium ion diffusion coefficient (D_{Na+}) in the bulk of the particles was calculated according to the plots in the low-frequency region and the results are displayed in Table S4. For the undoped and Mg^{2+}-doped samples, the diffusion coefficient of sodium ion at different temperatures is very similar, which means that Mg^{2+} doping has little influence on the diffusion coefficient of sodium ions in the bulk of the particle. Combined with the results of crystal volume change, interfacial resistance changes, and ion diffusion in the bulk, Mg^{2+} is mainly distributed on the surface of particles as illustrated in Figure 8.

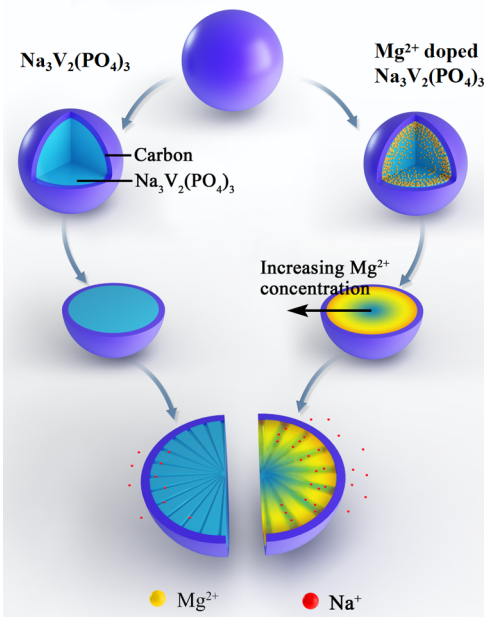

Figure 8. Schematic illustration of sodium ion diffusion channel in undoped and Mg^{2+}-doped $Na_3V_2(PO_4)_3/C$.

It is well-known that cation doping improves the electrochemical performance mainly because of the structural stability and enhanced ionic and electronic conductivity induced by the doped ion.[21,48,49] However, the enhanced electrochemical performance is also related to the doped ion distribution. Nonuniform distribution of Mg^{2+} may lead to stratification of $Na_3V_2(PO_4)_3$ particles. As shown in Figure 8, most of the Mg^{2+} are distributed on the particle surface layer and less Mg^{2+} are disseminated in the bulk of $Na_3V_2(PO_4)_3$ particle. This is further demonstrated in the Supporting Information. According to previous reports, cation doping can enlarge the Na ion diffusion pathway.[30] Hence, nonuniform distribution of Mg^{2+} doping brings out faster Na^+ diffusion on the surface than that in the bulk of the particle. At the same time, shown in the SEM image of $Na_3V_2(PO_4)_3/C$ from Figure S2, the microscale particle size hinders the electrochemical performance with the long ionic diffusion distance.[50] When batteries are cycled at high rates, it is hard for Na^+ to go into the bulk of $Na_3V_2(PO_4)_3/C$ particle because of the short time for such a long ionic diffusion distance. As a result, the electrochemical reaction occurs mainly on the surface of the particle. The surface property of active material is vital for electrochemical reaction since effective charge carriers must successfully diffuse to the surface and undergo interfacial charge transfer.[51] Therefore, the modified surface property for Mg^{2+}-doped samples leads to the superior electrochemical performance compared to that of the undoped sample.

4. CONCLUSIONS

In summary, a series of Na-rich $Na_{3+x}V_{2-x}Mg_x(PO_4)_3/C$ (x = 0, 0.05, and 0.1) cathode materials were synthesized by the sol–gel method. All doped samples display improved electrochemical performance, especially at high rates. To probe how Mg^{2+} doping affects the electrochemical performance of $Na_3V_2(PO_4)_3/C$, the doping site was explored by empirical formula, first-principles calculation, and ICP. The results indicate that Mg^{2+} prefers to go to the V site and extra Na^+ is introduced to $Na_3V_2(PO_4)_3/C$ crystal to keep the charge balance. Because the extra Na^+ is located in the Na(2) site, it not only increases the electrochemically active Na^+ content but also stabilizes the crystal structure. In addition, the distribution of Mg^{2+} in the $Na_3V_2(PO_4)_3/C$ particle also influences the electrochemical performance. Combined with the results of the crystal volume shifts, interfacial resistance changes, and ion diffusion in the bulk, it can be concluded that Mg^{2+} distributes on the surface of $Na_3V_2(PO_4)_3/C$ particle. This will facilitate the surface reaction during charging/discharging, leading to excellent rate performance of the material.

DOI: 10.1021/acs.chemmater.7b03903
Chem. Mater. XXXX, XXX, XXX−XXX

■ ASSOCIATED CONTENT

Supporting Information

The Supporting Information is available free of charge on the ACS Publications website at DOI: 10.1021/acs.chemmater.7b03903.

The crystal structure of $Na_3V_2(PO_4)_3$, the theoretical ratio of Na, V, Mg, and P when the doped site is V/Na site, ICP results for Mg^{2+}-doped $Na_3V_2(PO_4)_3$ samples, sodium diffusion coefficients of $Na_3V_2(PO_4)_3$/C and $Na_{3.05}V_{1.95}Mg_{0.05}(PO_4)_3$/C at different temperatures, SEM image of $Na_3V_2(PO_4)_3$ and STEM-HADDF images, and EDS line scan results of$Na_{3.05}V_{1.95}Mg_{0.05}(PO_4)_3$/C sample (PDF)

■ AUTHOR INFORMATION

Corresponding Authors

*E-mail: membrane@bit.edu.cn (Y.B.).
*E-mail: ongsp@eng.ucsd.edu (S.P.O.).
*E-mail: shirleymeng@ucsd.edu (Y.S.M.).
*E-mail: chuanwu@bit.edu.cn (C.W.).

ORCID

Hanmei Tang: 0000-0003-2659-7768
Ying Bai: 0000-0003-3645-4357
Shyue Ping Ong: 0000-0001-5726-2587
Ying Shirley Meng: 0000-0001-8936-8845
Chuan Wu: 0000-0003-3878-179X

Present Address

#Energy Storage and Distributed Resources Division, Lawrence Berkeley National Laboratory, Berkeley, California 94720, United States.

Notes

The authors declare no competing financial interest.

■ ACKNOWLEDGMENTS

The present work is supported by the National Basic Research Program of China (Grant No. 2015CB251100) and the Beijing Co-construction Project (20150939014). Hui Li is thankful for the support from the China Scholarship Council (File No. 201506030049). Y.S.M., C.M., and J.A. are grateful for financial support from the USA National Science Foundation under Award No. DMR1608968. J.A. acknowledges the AGEP GSR fellowship, which is a supplement fund to the DMR NSF award. S.P.O., H.T., and B.R. acknowledge funding from the U.S. Department of Energy, Office of Science, Basic Energy Sciences, under Award No. DE-SC0012118 for the computational portion of the work, as well as computing resources provided by Triton Shared Computing Cluster (TSCC) at the University of California, San Diego (UCSD), the National Energy Research Scientific Computing Center (NERSC), and the Extreme Science and Engineering Discovery Environment (XSEDE) supported by the National Science Foundation under Grant No. ACI-1053575. The authors thank Dr. Liqiang Zhang and Mr. Qiao Ni for their help with the STEM−EDS contributions.

■ REFERENCES

(1) Tarascon, J. M.; Armand, M. Issues and challenges facing rechargeable lithium batteries. *Nature* **2001**, *414*, 359−367.
(2) Slater, M. D.; Kim, D.; Lee, E.; Johnson, C. S. Sodium-ion batteries. *Adv. Funct. Mater.* **2013**, *23*, 947−958.
(3) Palomares, V.; Villaluenga, I.; Hueso, K. B.; Carretero-Gonzalez, J.; Rojo, T.; Serras, P. Na-ion batteries, recent advances and present challenges to become low cost energy storage systems. *Energy Environ. Sci.* **2012**, *5*, 5884−5901.
(4) Kim, S. W.; Seo, D. H.; Ma, X.; Ceder, G.; Kang, K. Electrode materials for eechargeable sodium-ion batteries: potential alternatives to current lithium-ion batteries. *Adv. Energy Mater.* **2012**, *2*, 710−721.
(5) Ong, S. P.; Chevrier, V. L.; Hautier, G.; Jain, A.; Moore, C.; Kim, S.; Ma, X.; Ceder, G. Voltage, stability and diffusion barrier differences between sodium-ion and lithium-ion intercalation materials. *Energy Environ. Sci.* **2011**, *4*, 3680−3688.
(6) Dunn, B.; Kamath, H.; Tarascon, J. M. Pseudocapacitive oxide materials for high-rate electrochemical energy storage. *Science* **2011**, *334*, 928−935.
(7) Cheng, F. Y.; Liang, J.; Tao, Z. L.; Chen, J. Functional materials for rechargeable batteries. *Adv. Mater.* **2011**, *23*, 1695−1715.
(8) Saravanan, K.; Mason, C. W.; Rudola, A.; Wong, K. H.; Balaya, P. The first report on excellent cycling stability and superior rate capability of $Na_3V_2(PO_4)_3$ for sodium ion batteries. *Adv. Energy Mater.* **2013**, *3*, 444−450.
(9) Shen, W.; Wang, C.; Liu, H. M.; Yang, W. S. Towards highly stable storage of sodium ions: a porous $Na_3V_2(PO_4)_3$/C cathode material for sodium-ion batteries. *Chem. - Eur. J.* **2013**, *19*, 14712−14718.
(10) Zhu, C. B.; Song, K. P.; van Aken, P. A.; Yu, Y.; Maier, J. Carbon-coated $Na_3V_2(PO_4)_3$ embedded in porous carbon matrix: an ultrafast Na-storage cathode with the potential of outperforming Li cathodes. *Nano Lett.* **2014**, *14*, 2175−2180.
(11) Li, S.; Dong, Y. F.; Xu, L.; Xu, X.; He, L.; Mai, L. Q. Effect of carbon matrix dimensions on the electrochemical properties of $Na_3V_2(PO_4)_3$ nanograins for high-performance symmetric sodium-ion batteries. *Adv. Mater.* **2014**, *26*, 3545−3553.
(12) Li, H.; Bai, Y.; Wu, F.; Li, Y.; Wu, C. Budding willow branches shaped $Na_3V_2(PO_4)_3$/C nanofibers synthesized via an electrospinning technique and used as cathode material for sodium ion batteries. *J. Power Sources* **2015**, *273*, 784−792.
(13) Jian, Z. L.; Han, W.; Lu, X.; Yang, H.; Hu, Y. S.; Zhou, J.; Zhou, Z.; Li, J.; Chen, W.; Chen, D.; Chen, L. Sodium-ion batteries: superior electrochemical performance and storage mechanism of $Na_3V_2(PO_4)_3$ cathode for room-temperature sodium-ion batteries. *Adv. Energy Mater.* **2013**, *3*, 156−160.
(14) Fang, Y. J.; Xiao, L. F.; Ai, X. P.; Cao, Y. L.; Yang, H. X. Hierarchical carbon framework wrapped $Na_3V_2(PO_4)_3$ as a superior high-rate and extended lifespan cathode for sodium-ion batteries. *Adv. Mater.* **2015**, *27*, 5895.
(15) Li, H.; Bai, Y.; Wu, F.; Ni, Q.; Wu, C. $Na_3V_2(PO_4)_3$C nanorods as advanced cathode material for sodium ion batteries. *Solid State Ionics* **2015**, *278*, 281−286.
(16) Du, K.; Guo, H.; Hu, G.; Peng, Z.; Cao, Y. $Na_3V_2(PO_4)_3$ as cathode material for hybrid lithium ion batteries. *J. Power Sources* **2013**, *223*, 284−288.
(17) Fei, H. L.; Wu, X. M.; Li, H.; Wei, M. D. Novel sodium intercalated $(NH_4)_2V_6O_{16}$ platelets: High performance cathode materials for lithium-ion battery. *J. Colloid Interface Sci.* **2014**, *415*, 85−88.
(18) Tao, S.; Cui, P. X.; Huang, W. F.; Yu, Z.; Wang, X. B.; Wei, S. H.; Liu, D. B.; Song, L.; Chu, W. S. Sol−gel design strategy for embedded $Na_3V_2(PO_4)_3$ particles into carbon matrices for high-performance sodium-ion batteries. *Carbon* **2016**, *96*, 1028−1033.
(19) Li, H.; Bi, X. X.; Bai, Y.; Yuan, Y. F.; Shahbazian-Yassar, R.; Wu, C.; Wu, F.; Lu, J.; Amine, K. High-rate, durable sodium-ion battery cathode enabled by carbon-coated micro-sized $Na_3V_2(PO_4)_3$ particles with interconnected cerical nanowalls. *Adv. Mater. Interfaces* **2016**, *3*, 1500740.
(20) Wang, W.; Jiang, B.; Hu, L. W.; Lin, Z. S.; Hou, J. G.; Jiao, S. Q. Single crystalline VO_2 nanosheets: A cathode material for sodium-ion batteries with high rate cycling performance. *J. Power Sources* **2014**, *250*, 181−187.

DOI: 10.1021/acs.chemmater.7b03903
Chem. Mater. XXXX, XXX, XXX−XXX

(21) Chung, S. Y.; Bloking, T. J.; Chiang, Y. M. Electronically conductive phospho-olivines as lithium storage electrode. *Nat. Mater.* **2002**, *1*, 123−128.
(22) Li, H.; Wu, C.; Bai, Y.; Wu, F.; Wang, M. Z. Controllable synthesis of high-rate and long cycle-life $Na_3V_2(PO_4)_3$ for sodium-ion batteries. *J. Power Sources* **2016**, *326*, 14−22.
(23) Li, H.; Yu, X. Q.; Bai, Y.; Wu, F.; Wu, C.; Liu, L.-Y.; Yang, X.-Q. Effects of Mg doping on remarkably enhanced electrochemistry performances of $Na_3V_2(PO_4)_3$ cathode material for sodium ion batteries. *J. Mater. Chem. A* **2015**, *3*, 9578−9586.
(24) Aragon, M. J.; Lavela, P.; Ortiz, G. F.; Tirado, J. L. Effect of iron substitution in the electrochemical performance of $Na_3V_2(PO_4)_3$ as cathode for Na-ion batteries. *J. Electrochem. Soc.* **2015**, *162*, A3077−A3083.
(25) Aragon, M. J.; Lavela, P.; Ortiz, G. F.; Tirado, J. L. Benefits of chromium substitution in $Na_3V_2(PO_4)_3$ as a potential candidate for sodium-ion batteries. *ChemElectroChem* **2015**, *2*, 995−1002.
(26) Aragón, M. J.; Lavela, P.; Alcántara, R.; Tirado, J. L. Effect of aluminum doping on carbon loaded $Na_3V_2(PO_4)_3$ as cathode material for sodium-ion batteries. *Electrochim. Acta* **2015**, *180*, 824−830.
(27) Klee, R.; Lavela, P.; Aragon, M. J.; Alcantara, R.; Tirado, J. L. Enhanced high-rate performance of manganese substituted $Na_3V_2(PO_4)_3$/C as cathode for sodium-ion batteries. *J. Power Sources* **2016**, *313*, 73−80.
(28) Shen, W.; Li, H.; Guo, Z. Y.; Li, Z. H.; Xu, Q. J.; Liu, H. M.; Wang, Y. G. Improvement on the high-rate performance of Mn-doped $Na_3V_2(PO_4)_3$ as a cathode material for sodium ion batteries. *RSC Adv.* **2016**, *6*, 71581−71588.
(29) Zhu, C. B.; Song, K. P.; van Aken, P. A.; Maier, J.; Yu, Y. Carbon-coated $Na_3V_2(PO_4)_3$ embedded in porous carbon matrix: an ultrafast Na-storage cathode with the potential of outperforming Li cathodes. *Nano Lett.* **2014**, *14*, 2175−2180.
(30) Li, H.; Bai, Y.; Wu, F.; Ni, Q.; Wu, C. Na-rich $Na_{3+x}V_{2-x}Ni_x(PO_4)_3$/C for sodium ion batteries: controlling the doping site and improving the electrochemical performances. *ACS Appl. Mater. Interfaces* **2016**, *8*, 27779−27787.
(31) Kresse, G.; Furthmüller, J. Efficient iterative schemes for ab initio total-energy calculations using a plane-wave basis set. *Phys. Rev. B: Condens. Matter Mater. Phys.* **1996**, *54*, 11169−11186.
(32) Blöchl, P. E. Projector agmented-wave method. *Phys. Rev. B: Condens. Matter Mater. Phys.* **1994**, *50*, 17953−17979.
(33) Perdew, J. P. J.; Burke, K.; Ernzerhof, M. Generalized gradient approximation made simple. *Phys. Rev. Lett.* **1996**, *77*, 3865−3868.
(34) Ong, S. P.; Richards, W. D.; Jain, A.; Hautier, G.; Kocher, M.; Cholia, S.; Gunter, D.; Chevrier, L.; Persson, K. a.; Ceder, G. Python materials genomics (pymatgen): A robust, open-source python library for materials analysis. *Comput. Mater. Sci.* **2013**, *68*, 314−319.
(35) Bergerhoff, G.; Hundt, R.; Sievers, R.; Brown, D. I. The inorganic crystal structure data base. *J. Chem. Inf. Model.* **1983**, *23*, 66−69.
(36) Deng, Z.; Zhu, Z.; Chu, I. H.; Ong, S. P. Data-driven first-principles methods for the study and design of alkali superionic conductors. *Chem. Mater.* **2017**, *29*, 281−288.
(37) Hart, G. L. W.; Forcade, R. W. Algorithm for generating derivative structures. *Phys. Rev. B: Condens. Matter Mater. Phys.* **2008**, *77*, 224115.
(38) Ong, S. P.; Wang, L.; Kang, B.; Ceder, G. Li-Fe-P-O_2 phase diagram from first principles calculations. *Chem. Mater.* **2008**, *20*, 1798−1808.
(39) Jain, A.; Ong, S. P.; Hautier, G.; Chen, W.; Richards, W. D.; Dacek, S.; Cholia, S.; Gunter, D.; Skinner, D.; Ceder, G.; Persson, K. A. Commentary: The materials project: A materials genome approach to accelerating materials innovation. *APL Mater.* **2013**, *1*, 011002.
(40) Ong, S. P.; Cholia, S.; Jain, A.; Brafman, M.; Gunter, D.; Ceder, G.; Persson, K. a. The materials application programming interface (API): A simple, flexible and efficient API for materials data based on REpresentational State Transfer (REST) principles. *Comput. Mater. Sci.* **2015**, *97*, 209−215.
(41) Wei, S. H.; Zhang, S. Chemical trends of defect formation and doping limit in II-VI semiconductors: The case of CdTe. *Phys. Rev. B: Condens. Matter Mater. Phys.* **2002**, *66*, 15521.
(42) Zhu, Z.; Chu, I. H.; Deng, Z.; Ong, S. P. Role of Na^+ interstitials and dopants in enhancing the Na^+ conductivity of the cubic Na_3PS_4 superionic conductor. *Chem. Mater.* **2015**, *27*, 8318−8325.
(43) Chung, S. Y.; Chiang, Y. M. Microscale measurements of the electrical conductivity of Doped $LiFePO_4$. *Electrochem. Solid-State Lett.* **2003**, *6*, A278−A281.
(44) Meethong, N.; Kao, Y. H.; Speakman, S. A.; Chiang, Y. M. Aliovalent doping for improved battery performance: aliovalent substitutions in olivine lithium iron phosphate and impact on structure and properties. *Adv. Funct. Mater.* **2009**, *19*, 1060−1070.
(45) Li, K.; Shao, J.; Xue, D. Calculation of impurity energy levels of transition metal ions in inorganic crystals based on electronegativity. *Mater. Res. Innovations* **2013**, *17*, 218−223.
(46) Han, D. W.; Lim, S. J.; Kim, Y. I.; Kang, S. H.; Lee, Y. C.; Kang, Y. M. Facile lithium ion transport through superionic pathways formed on the surface of $Li_3V_2(PO_4)_3$/C for high power Li-ion battery. *Chem. Mater.* **2014**, *26*, 3644−3650.
(47) Shen, W.; Wang, C.; Xu, Q. J.; Liu, H. M.; Wang, Y. G. Nitrogen-doping-induced defects of a carbon coating layer facilitate Na-storage in electrode materials. *Adv. Energy Mater.* **2015**, *5*, 1400982.
(48) Wang, B.; Xu, B. H.; Liu, T. F.; Liu, P.; Guo, C. F.; Wang, S.; Wang, Q. M.; Xiong, Z. G.; Wang, D. L.; Zhao, X. S. Mesoporous carbon-coated $LiFePO_4$ nanocrystals co-modified with graphene and Mg^{2+} doping as superior cathode materials for lithium ion batteries. *Nanoscale* **2014**, *6*, 986−995.
(49) Park, K. S.; Xiao, P.; Kim, S. Y.; Dylla, A.; Choi, Y. M.; Henkelman, G.; Stevenson, K. J.; Goodenough, J. B. Enhanced charge-transfer kinetics by anion surface modification of $LiFePO_4$. *Chem. Mater.* **2012**, *24*, 3212−3218.
(50) Wu, Y. M.; Wen, Z. H.; Li, J. H. Hierarchical carbon-coated $LiFePO_4$ nanoplate microspheres with high electrochemical performance for Li-ion batteries. *Adv. Mater.* **2011**, *23*, 1126−1129.
(51) Li, G. Y.; Huang, Z. L.; Zuo, Z. C.; Zhang, Z. J.; Zhou, H. H. Understanding the trace Ti surface doping on promoting the low temperature performance of $LiNi_{1/3}Co_{1/3}Mn_{1/3}O_2$ cathode. *J. Power Sources* **2015**, *281*, 69−76.

DOI: 10.1021/acs.chemmater.7b03903
Chem. Mater. XXXX, XXX, XXX−XXX